



# Facile synthesis of Mn/N-doped TiO<sub>2</sub> on wood-based activated carbon fiber as an efficient visible-light-driven photocatalyst

Dongna Li<sup>1</sup> , Yin Chen<sup>1</sup> , Fen Yin<sup>1</sup> , Lizhi Zhu<sup>1</sup> , Jianing Li<sup>2</sup> , and Xiaojun Ma<sup>1,\*</sup>

<sup>1</sup> College of Packaging and Printing Engineering, Tianjin University of Science & Technology, Tianjin 300222, People's Republic of China

<sup>2</sup> Ministry of Agriculture Key Laboratory of Biology and Genetic Resource Utilization of Rubber Tree/State Key Laboratory Breeding Base of Cultivation and Physiology for Tropical Crops, Rubber Research Institute, Chinese Academy of Tropical Agricultural Sciences, Danzhou 571737, People's Republic of China

Received: 16 April 2018

Accepted: 9 May 2018

Published online:

16 May 2018

© Springer Science+Business Media, LLC, part of Springer Nature 2018

## ABSTRACT

The exploration of highly efficient and stable visible-light-driven photocatalysts for wastewater treatment has been recognized as one of the most challenging topics in environmental remediation. In this study, we report a new type of Mn/N co-doped TiO<sub>2</sub> supported on wood-based activated carbon fiber (Mn-N/TiO<sub>2</sub>-WACF) composite material that can be synthesized via sol-gel method. XRD indicates that the nano-TiO<sub>2</sub> particles in the composites are in the anatase phase (except when calcined at 850 °C) and the average crystallite size is approximately 23–33 nm. Doping with Mn and N significantly inhibits the crystal phase transformation of TiO<sub>2</sub> from anatase to rutile. Photocatalytic experiments confirm that the Mn-N/TiO<sub>2</sub>-WACF catalysts are highly efficient and robust for the photodegradation of methylene blue under visible light irradiation ( $\lambda > 420$  nm). Mn-N/TiO<sub>2</sub>-WACF exhibits the highest photocatalytic activity (reaches 99%) after calcined at 550 °C. The introduction of Mn and N not only improves the light adsorption and redox activity of TiO<sub>2</sub>, but also promotes photochemical stability because of narrow band gap energy and lower recombination rate of photoinduced electron-hole pairs. Composite photocatalysts such as these materials are important in the ongoing effort to design and explore new low cost, high efficiency, robust photocatalytic materials.

## Introduction

Currently, the rapidly developing printing and dye industries are introducing a variety of environmentally harmful dyes and chemicals into wastewater

[1, 2]. This waste is extremely diverse and has complex compositions that are both high colored and poorly biodegradable. These pollutants represent a major global problem and wastewater treatment remains a difficult challenge. Traditional physical

Address correspondence to E-mail: mxj75@tust.edu.cn

<https://doi.org/10.1007/s10853-018-2429-7>

adsorption, chemical decomposition and biodegradation methods have inherent limitations such as the need for complex equipment, a narrow application range, high energy consumption, low efficiency, incomplete degradation of pollutants, and so on. Therefore, many attempts have focused on finding a green pollution-control technology that is economical and efficient and has wide range of applications that will satisfy future demands.

Semiconductor photocatalysts are promising because they are safe, solid-phase materials that are resistant to deactivation, chemically stable and environmentally friendly [3–5]. Heterogeneous photocatalysts have been recognized as optimal materials for this application due to the success of TiO<sub>2</sub>. TiO<sub>2</sub> has numerous qualities that are superior to those of other materials, including a high photocatalytic efficiency, low cost and non-toxicity [6], all of which are considered attractive characteristics for the degradation of organic pollutants in wastewater. However, TiO<sub>2</sub> only exhibits photocatalytic activity under UV light (wavelength  $\lambda < 380$  nm), which accounts for only 5% of the energy from the solar spectrum [7]. In addition, the quantum efficiency of TiO<sub>2</sub> is quite low, and photoinduced electron–hole pairs generated in TiO<sub>2</sub> can easily recombine. To enhance the visible-light absorption and reduce the recombination of photoinduced electron–hole pairs in TiO<sub>2</sub>, a variety of studies have been performed using modified TiO<sub>2</sub> treatment methods. These studies showed that metal and non-metal dopants were some of the most effective modification methods for TiO<sub>2</sub> [8–10]. Metal doping could create potential traps for photoinduced electron–hole pairs that effectively separate them; it could also reduce the band gap and broaden the light-response range of TiO<sub>2</sub>. Among the non-metal dopants, N has the obvious advantages of a small ionic radius, a high thermal stability, and low number of recombination centers [11, 12]. Unlike pure TiO<sub>2</sub>, doped TiO<sub>2</sub> can use visible light to initiate photocatalysis.

Furthermore, powder-based TiO<sub>2</sub> particles suffer from several disadvantages that restrict their practical application, including easy agglomeration and difficult separation and recycling processes. More recently, numerous studies have focused on achieving an optimal-support for the photocatalyst. The preparation of TiO<sub>2</sub> photocatalysts deposited on suitable, high surface area support materials has shown promising results. Activated carbon fiber

(ACF) has been established as a promising support material with a large specific surface area and fast adsorption and desorption [13–16]. In our previous study, nano-TiO<sub>2</sub> was loaded onto the surface of wood-based activated carbon fiber (WACF). Using a synergistic reaction, the photocatalytic efficiency was improved under UV irradiation [17]. Currently, to load the ACF, most methods synthesize ion-doped TiO<sub>2</sub> by only a single ion doping method of either metal ions or non-metal ions [18–20]. However, to our knowledge, very little work has been conducted on co-doping.

Based on the above considerations and our previous work [21, 22], the objective of this study was to investigate the use of WACF as a substrate to immobilize Mn/N co-doped TiO<sub>2</sub> (Mn–N/TiO<sub>2</sub>-WACF) in order to enhance the visible-light photocatalytic activity via a sol–gel method. The surface morphology, phase structure, chemical states, optical absorption and photocatalytic activity of Mn–N/TiO<sub>2</sub>-WACF at different calcination temperatures have been discussed. This study also provides examples of industrial applications for the treatment of wastewater from the printing and dye.

## Materials and methods

### Materials

Chinese fir (*Cunninghamia lanceolata*) was used as the raw material. The debarked chips were ground, and the powder, which had a 20–80 mesh size, was dried in an oven at 105 °C for 24 h prior to being used. All chemicals and reagents used in this experiment were of analytical grade and were used without any further purification.

### Preparation of photocatalytic composite material

#### *Preparation of WACF*

A mixture composed of dried Chinese Fir powder (20–80 mesh) and phenol at a mass ratio of 1:6 was liquefied for 2.5 h at 160 °C with 8% phosphoric acid (based on the mass ratio of phenol). The as-prepared liquefied wood was placed into a reaction tube with 5% hexamethylenetetramine (based on the mass ratio of liquefied wood) as the synthetic material. The

mixture was heated from room temperature to 130 °C in 40 min to prepare the spinning solution, and was placed into a spinning machine. The initial fibers were prepared by melt-spinning.

After melt-spinning, the spun filaments were cured by soaking in an acid solution HCHO and HCl as main components at 95 °C for 4 h, washed with deionized water and finally dried at 90 °C for 2 h. The precursors were activated for 40 min by heating from room temperature to different activation temperature at a heating rate of 5 °C/min under 200 ml/min stream of N<sub>2</sub> and 8 g/min flow rate of steam. WACF materials from liquefied wood were prepared [23–25].

### Preparation of Mn–N/TiO<sub>2</sub>-WACF

The detailed preparation process is described as follows. Under moderate stirring, a mixed solution composed of 2.182 ml of distilled water, 2 ml of acetic acid and 30 ml of absolute ethanol was dissolved in 3 ml of MnSO<sub>4</sub>·H<sub>2</sub>O (17 g/l). Afterward, for N-doping, all of the above solutions and 0.3 g of urea were slowly added into a mixed solution containing 60 ml of absolute ethanol and 10.2 g of tetrabutyl titanate, and stirred vigorously until they were completely homogenous. They were aged in a water bath at 40 °C for 2 h to obtain a milky white colloidal solution. The prepared WACF was placed in the solution and vibrated for 30 min. After a certain time of continuous dipping, the fibers were dried at 105 °C for 2 h, and calcined in N<sub>2</sub> atmosphere (100 ml/min) for several hours (the calcination temperatures were 450, 550, 650, 750, 850 °C), and then naturally cooled to give the Mn–N/TiO<sub>2</sub>-WACF photocatalytic material. The as-prepared samples were referred to as Mn–N/TiO<sub>2</sub>-WACF-450; Mn–N/TiO<sub>2</sub>-WACF-550; Mn–N/TiO<sub>2</sub>-WACF-650; Mn–N/TiO<sub>2</sub>-WACF-750 and Mn–

N/TiO<sub>2</sub>-WACF-850, according to their respective calcination temperatures. A schematic of the production process is shown in Fig. 1.

### Characterization of Mn–N/TiO<sub>2</sub>-WACF

The surface morphologies of Mn–N/TiO<sub>2</sub>-WACF were examined via SEM (JSM-7500F, JEOL) with an acceleration voltage of 10 keV.

The X-ray diffraction (XRD) analyses were carried out at room temperature on a power X-ray diffractometer (D/max-2500, Japan, Rigaku) using Cu K $\alpha$  radiation (wavelength of 0.154 nm, powdered samples). The XRD analysis conditions were as follows: scanning range of 20°–80°, scanning rate of 8°/min at 40 kV and 100 mA.

The average crystallite size ( $D$ ) of anatase TiO<sub>2</sub> is calculated using Scherrer's equation:

$$D = 0.89\lambda/\beta \cos \theta \quad (1)$$

where  $\lambda$  is X-ray wavelength (0.154 nm),  $\theta$  is Bragg angle of diffraction peaks (°), and  $\beta$  is full width at half maximum.

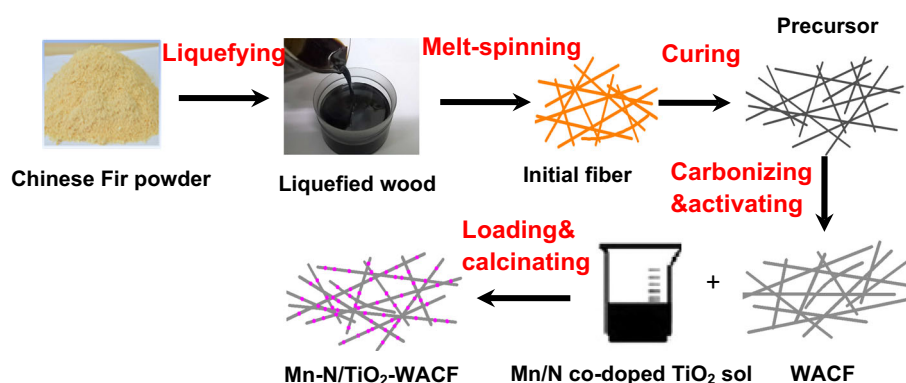
The content of anatase TiO<sub>2</sub> is calculated as followed:

$$X_A = I_A/(I_A + 1.265/I_R) \quad (2)$$

where  $I_A$  and  $I_R$  are the peak intensities of the anatase (101) plane and rutile (110) plane, respectively.

XPS measurements of the samples at various calcination temperatures were performed using a Kratos Axis Ultra DLD multi-technique X-ray photoelectron spectrometer, and the data were collected using the Al K $\alpha$  X-ray beam ( $h\nu = 1486.6$  eV). XPS survey spectra were recorded with a pass energy of 80 eV, and the high-resolution spectra were obtained with a pass energy of 40 eV. The C 1s signal of 284.6 eV was used to calibrate the XPS data. Atomic ratios were

**Figure 1** Schematic of production process of Mn–N/TiO<sub>2</sub>-WACF.



calculated from the XPS spectra after correcting the relative peak areas by sensitivity factors according to the transmission characteristics of the physical electronics SCA. A nonlinear least squares curve-fitting program (CasaXPS software) was used for XPS spectral deconvolution.

The photocatalytic properties of the prepared Mn–N/TiO<sub>2</sub>-WACF were measured with a UV-3600 spectrophotometer (Shimadzu, Kyoto, Japan). The diffuse reflectance spectra of the samples were recorded over a range of 200–800 nm at room temperature in air from 200 to 700 nm.

A F4500 photoluminescence spectrometer (Hitachi, Japan) was used to characterize the photoluminescence (PL) spectra of the samples and was excited at the wavelength of 245 nm.

#### Photocatalytic activity measurement

Photocatalytic activity testing was performed in a homemade photocatalytic reaction device (in a darkroom with a tungsten halogen lamp and a magnetic stirring apparatus). Up to 10 mg of shredded sample was dispersed in 100 ml of a methylene blue (MB) solution (33 mg/l) and stirred for 40 min in a darkroom to allow the system to reach an adsorption/desorption equilibrium between the samples and the MB molecules prior to irradiation. A 65 W tungsten halogen lamp with a 400 nm cutoff filter was used as the visible light source. The distance between the strip lamp and the fluid level was constant at 15 cm. After a period of illumination, the

absorbance of the supernatant solution was determined by measuring the UV–Vis absorbance at a wavelength of 665 nm. The degradation rate of MB was calculated using the following equation:

$$D = (A_0 - A)/A_0 \times 100\% \quad (3)$$

where  $A_0$  is the solution content before illumination, and  $A$  is the solution content after illumination at a particular time.

## Results and discussion

### Morphological characteristics of Mn–N/TiO<sub>2</sub>-WACF

The SEM images of WACF and Mn–N/TiO<sub>2</sub>-WACF are shown in Fig. 2. It can be clearly seen that WACF (Fig. 2a) has a smooth surface without surface deposits, and maintains a porous structure on both the inner and outer surfaces. Figure 2b–d shows that Mn, N co-doped TiO<sub>2</sub> possesses packed fine granular nanostructures dispersed throughout the composites as flakes and lumps, indicating that the composite structure of the photocatalytic materials is excellent. However, cracking and shedding of the doped TiO<sub>2</sub> are observed due to the inconsistent shrinkage between TiO<sub>2</sub> and the surface of WACF during calcination. Figure 2e, f, h shows that the Mn, N co-doped TiO<sub>2</sub> is discontinuous on the surface of WACF. The abundant pore structure of WACF is well preserved (Fig. 2i) and provides favorable conditions for

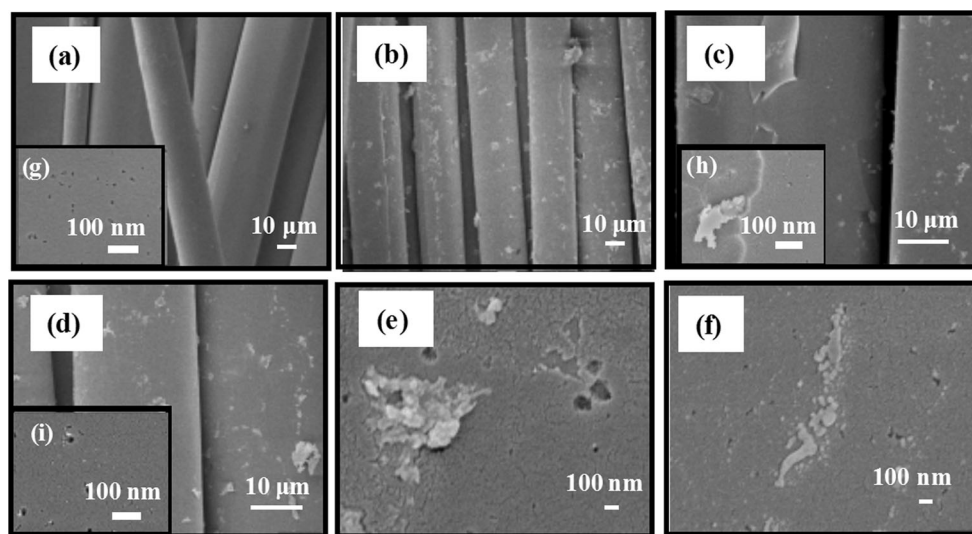


**Figure 2** SEM micrograph of a, g WACF and b–f, h, i Mn–N/TiO<sub>2</sub>-WACF.

the adsorption and photodegradation processes. In addition, relatively large aggregates of TiO<sub>2</sub> particles are deposited onto the surface of Mn–N/TiO<sub>2</sub>-WACF during the reaction.

### XRD analysis of Mn–N/TiO<sub>2</sub>-WACF

Figure 3 shows XRD patterns of Mn–N/TiO<sub>2</sub>-WACF at various calcination temperatures. As shown in Fig. 3, Mn–N/TiO<sub>2</sub>-WACF-450 and Mn–N/TiO<sub>2</sub>-WACF-550 contain only anatase TiO<sub>2</sub> without impurity phases, indicating that Mn and N are successfully doped into the lattice of TiO<sub>2</sub>, or are well dispersed. The observed peaks at  $2\theta = 25.2^\circ, 37.8^\circ, 48.2^\circ, 54.1^\circ, 55.1^\circ, 62.9^\circ, 69.5^\circ, 70.6^\circ$  and  $75.2^\circ$  can be indexed to the (101), (004), (200), (105), (211), (204), (116), (220) and (215) planes, respectively. The obtained peaks match exactly with the pure anatase phase of TiO<sub>2</sub> (JCPDS card No: 73-1764). The illustration in Fig. 3 displays the corresponding (101) diffraction peaks of anatase TiO<sub>2</sub> for all samples (except for Mn–N/TiO<sub>2</sub>-WACF-850). The dopants make the diffraction peaks shift to the right, which may be caused by a lattice

distortion. Meanwhile, the (101) peak shows a clear broadening, corresponding to a smaller crystalline size. The calcination temperature of 650 °C is not only the highest temperature at which a highly crystalline pure anatase phase is achieved, but is also the starting point of the ATR (anatase-to-rutile) phase transformation. In contrast, Mn–N/TiO<sub>2</sub>-WACF-850 has completely transformed into the rutile phase. The occurrence of the dominant peaks at  $2\theta = 27.5^\circ, 36.0^\circ, 39.1^\circ, 41.2^\circ, 44.0^\circ, 54.4^\circ, 56.5^\circ, 62.96^\circ, 64.0^\circ, 68.9^\circ$  and  $69.7^\circ$  can be assigned to the (110), (101), (200), (111), (210), (211), (220), (002), (310), (301) and (112) crystallographic planes of rutile TiO<sub>2</sub>, respectively, indicating that the rutile phase becomes the main phase when the synthesized photocatalyst is calcined at this temperature. Presumably, ATR phase transformation occurs because of the higher calcination temperature.

Table 1 shows the average particle size and anatase, rutile content of Mn–N/TiO<sub>2</sub>-WACF. As the calcination temperature increases from 450 to 750 °C, the average crystallite size increases slightly from 23 nm to 33 nm, which only increases by 30.3%. The smaller particle size might be caused by the larger specific surface area of WACF and the even dispersion of the Mn, N co-doped TiO<sub>2</sub> particles on its surface without sufficient aggregation. As a result, Mn–N/TiO<sub>2</sub>-WACF exhibits better photocatalytic activities. In addition, for Mn–N/TiO<sub>2</sub>-WACF-750, a high phase transformation occurred, resulting in a combination of the anatase and the rutile phases with approximately 18% rutile content. The samples that are calcined at a temperature between 450 and 650 °C contain almost purely anatase-phase TiO<sub>2</sub>. Anatase TiO<sub>2</sub> generally performs better in photocatalytic experiments than rutile TiO<sub>2</sub>. The superior activities of anatase over rutile in photocatalysis can be attributed to many factors, such as better charge-carrier mobility, longer exciton diffusion, larger particle size of the rutile phase and higher band gaps [26, 27].

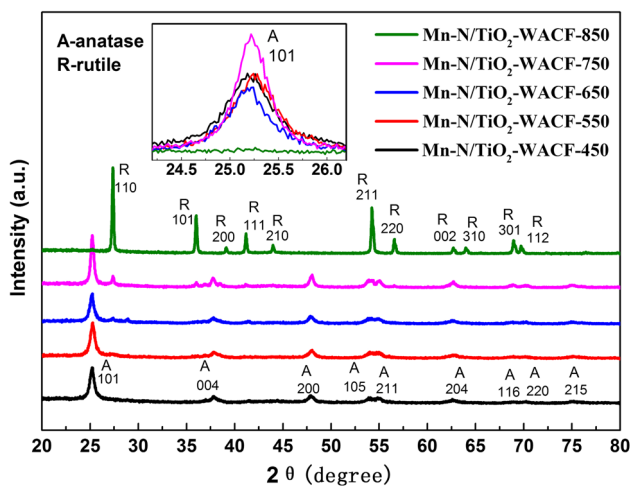


**Figure 3** XRD patterns of Mn–N/TiO<sub>2</sub>-WACF prepared at different temperatures.

**Table 1** Relationship between temperature and particle size, content of anatase, rutile TiO<sub>2</sub>

Samples	Mn–N/TiO <sub>2</sub> -WACF-450	Mn–N/TiO <sub>2</sub> -WACF-550	Mn–N/TiO <sub>2</sub> -WACF-650	Mn–N/TiO <sub>2</sub> -WACF-750	Mn–N/TiO <sub>2</sub> -WACF-850
Average crystallite size D (101) (nm)	23	23	25	33	–
Crystalline phase ratio (anatase/rutile) (%)	100/0	100/0	100/0	82/18	0/100

### XPS analysis of Mn–N/TiO<sub>2</sub>-WACF

XPS analysis of Mn, N/TiO<sub>2</sub>-WACF synthesized at various calcination temperatures is shown in Fig. 4. The full survey spectrum (Fig. 4a) demonstrates the presence of primarily C, O, Ti, Mn, N and P on the surface, indicating that Mn and N are well combined with the TiO<sub>2</sub> after a series of processes and have been successfully loaded onto the surface of WACF. Furthermore, the presence of P can be explained by the use of phosphoric acid catalyst for wood liquefaction.

The main elemental composition is shown in Table 2. C is the most abundant element, and changing the calcination temperature has little influence on the structure of WACF. The contents of Ti,

Mn and N first increase and then decrease as the calcination temperature increases and reach their maximal values of 6.05, 0.25 and 1.57% at 550, 650 and 650 °C, respectively. For Ti, the growth of the TiO<sub>2</sub> grain is beneficial for increased loading, and the resultant TiO<sub>2</sub> content increases between 450 and 550 °C. When the calcination temperature is excessively high, TiO<sub>2</sub> particles will be greatly consolidated and may even fall off from the support, resulting in a reduction in Ti content. The content of Mn and N increases as the calcination temperature increases from 450 to 650 °C, because anatase TiO<sub>2</sub> tends to be unstable, allowing the substitution of Mn and N for Ti and oxygen atoms in the TiO<sub>2</sub> lattice. At 850 °C, TiO<sub>2</sub> is transformed into a stable rutile phase,

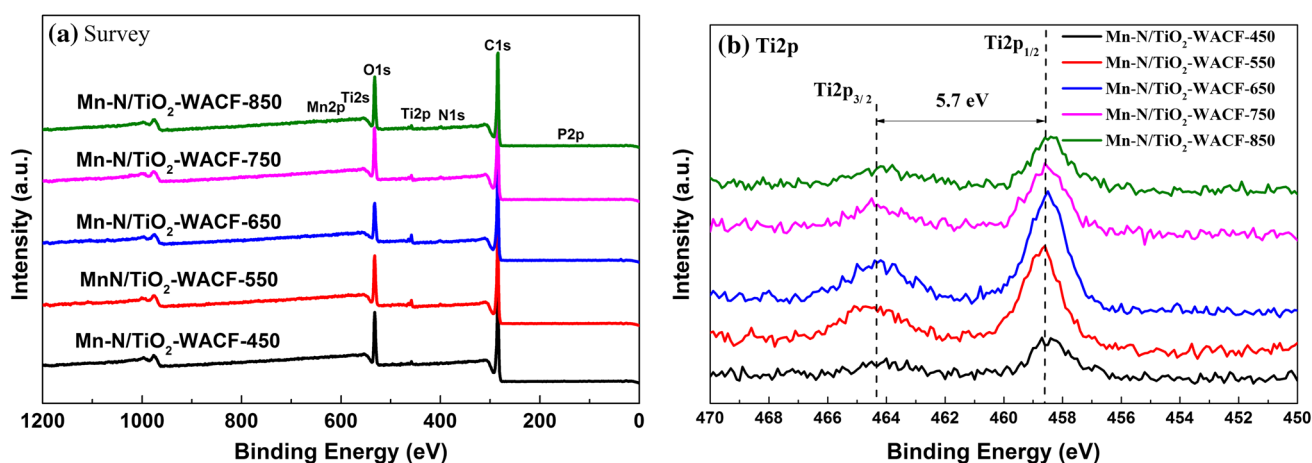


**Figure 4** XPS spectra of Mn–N/TiO<sub>2</sub>-WACF prepared at different temperatures and structure model: **a** full spectrum, **b** Ti 2*p*.

**Table 2** Global surface composition of Mn–N/TiO<sub>2</sub>-WACF prepared at different temperatures as determined by XPS

Samples	C1s		O1s		Ti2 <i>p</i>		Mn2 <i>p</i>		N1s		P2 <i>p</i>		O/C (%)
	BE (eV)	M (%)	BE (eV)	M (%)	BE (eV)	M (%)	BE (eV)	M (%)	BE (eV)	M (%)	BE (eV)	M (%)	
Mn–N/TiO <sub>2</sub> -WACF-450	284.4	75.76	532.0	22.18	458.7	1.21	639.8	0.10	395.0	0.67	131.9	0.08	29
Mn–N/TiO <sub>2</sub> -WACF-550	284.7	75.00	532.2	18.00	458.6	6.05	643.7	0.11	399.2	0.92	129.3	0.20	24
Mn–N/TiO <sub>2</sub> -WACF-650	284.5	76.60	532.1	17.91	458.5	3.52	639.0	0.25	399.9	1.57	131.9	0.16	23
Mn–N/TiO <sub>2</sub> -WACF-750	284.7	77.04	532.3	19.20	458.6	2.35	637.8	0.10	399.5	1.21	133.3	0.11	25
Mn–N/TiO <sub>2</sub> -WACF-850	284.6	76.10	532.0	21.09	458.4	1.60	641.9	0.08	399.6	0.89	133.0	0.24	28

which impedes the entry of Mn and N into the lattice, and causes their content to gradually decrease.

The peaks observed at 458.5 and 464.2 eV (Fig. 4b) can be assigned to  $Ti2p_{3/2}$  and  $Ti2p_{1/2}$ , respectively, with an energy level interval of 5.7 eV, indicating that the Ti in the samples is in the  $Ti^{4+}$  state ( $TiO_2$ ) [28]. To understand the chemical bonding states, the measurements of the high-resolution XPS spectra over the C1s, O1s, and N1s regions are conducted for the samples. Figure 5a illustrates the optimized curve-

fitting of the high-resolution XPS C1s spectra for all samples, and Table 3 shows the calculated percentages of non-functional and functional carbon atoms. We find that the C1s spectra are decomposed into a maximum of five identified components: the graphitic carbon (C–C, BE = 284.4–284.7 eV); carbon presented in phenolic, alcohol, ether or C=N groups (BE = 286.4–286.8 eV); carbonyl or quinone groups (C=O, BE = 287.3–287.5 eV); carboxyl, lactone, or ester groups (BE = 288.6–288.9 eV); and carbonate

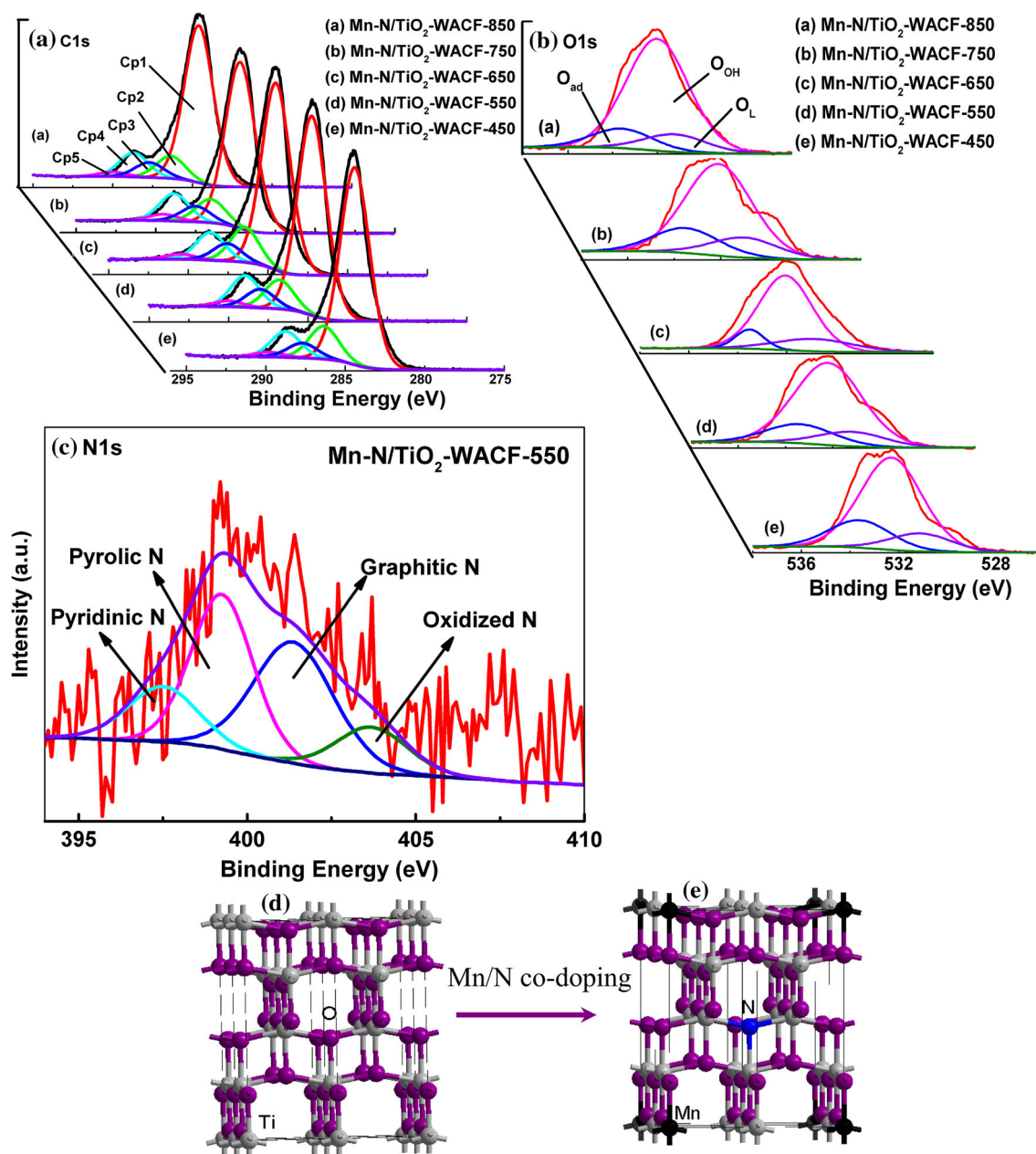


**Figure 5** XPS spectra of Mn–N/TiO<sub>2</sub>-WACF prepared at different temperatures: **a** XPS analysis on C1s of all series; **b** XPS analysis on O1s of all series; **c** XPS analysis on N1s; **d** anatase TiO<sub>2</sub> structure model; **e** Mn-, N-doped TiO<sub>2</sub> structure model.

**Table 3** Fitting results of the C1s regions of Mn–N/TiO<sub>2</sub>-WACF prepared at different temperatures

Samples	Graphite (C–C) (C <sub>P1</sub> )		C–O (C <sub>P2</sub> )		C=O (C <sub>P3</sub> )		C–OOH (C <sub>P4</sub> )		Carbonate groups (C <sub>P5</sub> )	
	BE (eV)	M (%)	BE (eV)	M (%)	BE (eV)	M (%)	BE (eV)	M (%)	BE (eV)	M (%)
Mn–N/TiO <sub>2</sub> -WACF-450	284.4	70.75	286.4	12.35	287.3	5.75	288.8	9.19	289.5	1.96
Mn–N/TiO <sub>2</sub> -WACF-550	284.7	70.76	286.8	11.0	287.5	5.92	288.9	10.04	290.1	2.28
Mn–N/TiO <sub>2</sub> -WACF-650	284.5	70.12	286.5	10.49	287.3	6.02	288.6	11.39	290.5	1.98
Mn–N/TiO <sub>2</sub> -WACF-750	284.7	69.95	286.6	10.04	287.4	6.66	288.8	11.65	290.4	1.7
Mn–N/TiO <sub>2</sub> -WACF-850	284.6	67.11	286.4	12.44	287.3	7.41	288.7	10.82	289.7	2.22

groups (BE = 289.5–290.5 eV) [29]. The C (C<sub>P1</sub>) is predominant in the C1s region. A decrease in C (C<sub>P1</sub>) and an increase in C (C<sub>P3</sub>) suggest that with increased temperature, the amount of graphitic carbon involved in the reaction increases, which brakes C–C bonds and forms C–O or C=O bonds. The C–O bonds then partially turn into more C–N bonds, resulting in the decrease of C–O content.

The optimized curve-fittings of the O1s peak for all samples are shown in Fig. 5b. Three different O functionalities can be identified. The peaks at 530.8–531.1, 532–532.3 and 533.4–533.6 eV correspond to O<sub>L</sub> (lattice oxygen), O<sub>OH</sub> (hydroxyl oxygen), and O<sub>ad</sub> (adsorbed oxygen), respectively [30]. The quantified area percentages of oxygen-containing functional groups are shown in Table 4. As the calcination temperature increases, the O<sub>L</sub> content of the samples first decreases and increases. In contrast, the O<sub>OH</sub> contents decrease and the O<sub>ad</sub> contents increase as the calcinations temperature increases. These results are probably caused by the N-substitution of oxygen atoms in the TiO<sub>2</sub> lattice, the increased removal of water molecules contained in the samples at higher calcination temperatures and the reaction of the doped N with O<sub>ad</sub> to form NO<sub>x</sub> during the calcination process, respectively.

Curve-fitting of the high-resolution XPS N1s spectra for Mn, N/TiO<sub>2</sub>-WACF-550 (Fig. 5c) shows that the N1s spectra decompose into a maximum of four identified components: pyridinic N (BE = 397.8 eV),

pyrrolic N (BE = 400.3 eV), graphitic N (BE = 401.3 eV) and oxidized N (BE = 4013.7 eV). The pyrrolic N and graphitic N are the predominant N-functionalities. Because the binding energies of Ti–N and pyridinic N are close, we could observe only one combined peak [31, 32].

The N peaks at the binding energies listed above confirm that the doping is successful and N replaced O atoms within the TiO<sub>2</sub> lattice. To analyze this replacement in detail, the anatase TiO<sub>2</sub> crystal with a 2 × 2 × 1 supercell model is studied. The supercell is built by stacking four anatase TiO<sub>2</sub> unit cells together. The supercell contains 48 atoms in total with 16 titanium atoms and 32 oxygen atoms as shown in Fig. 5d. The O atom at the center of the supercell is the doping site and substituted with blue N atoms. Similarly, doping sites of Ti atoms are shown with black Mn atoms (Fig. 5e).

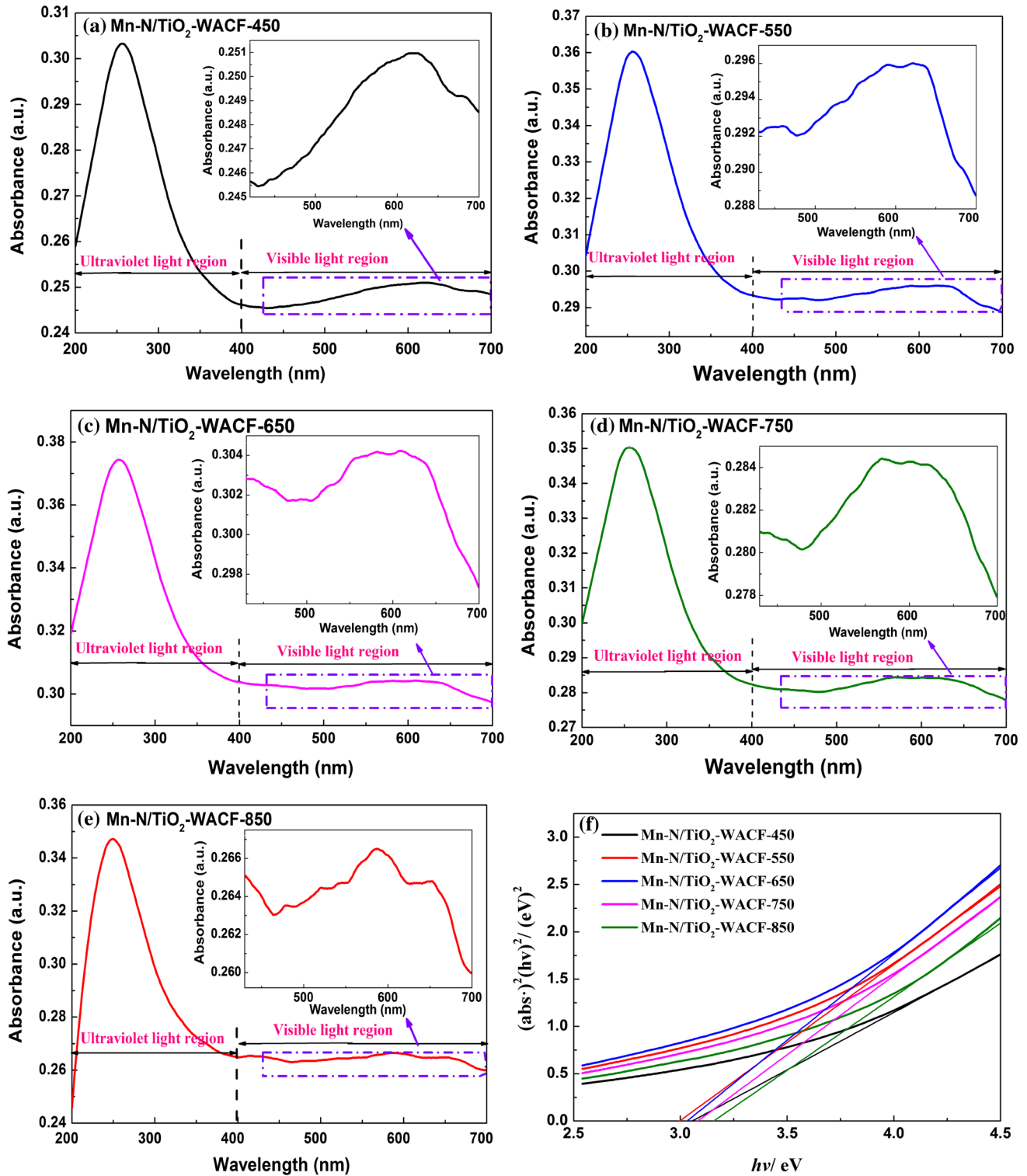
### UV-Vis spectrometry

Figure 6a–e shows the UV-Vis spectra of all the synthesized samples and can be used to investigate the use of solar energy during the photocatalytic reaction. The absorption patterns observed at wavelengths from 400 to 700 nm indicate strong optical responses to visible light irradiation after the addition of Mn and N. Mn–N/TiO<sub>2</sub>-WACF-450 shows the lowest absorptivity, which may indicate that the formed anatase grains and loading rate of TiO<sub>2</sub> are

**Table 4** Fitting results of the O1s regions of Mn–N/TiO<sub>2</sub>-WACF prepared at different temperatures

Samples	O <sub>L</sub>		O <sub>OH</sub>		O <sub>ad</sub>	
	BE (eV)	M (%)	BE (eV)	M (%)	BE (eV)	M (%)
Mn–N/TiO <sub>2</sub> -WACF-450	530.8	17.45	532.1	72.51	533.5	10.04
Mn–N/TiO <sub>2</sub> -WACF-550	531.2	12.58	532.2	70.99	533.4	16.44
Mn–N/TiO <sub>2</sub> -WACF-650	531.0	11.88	532.1	67.17	533.5	18.19
Mn–N/TiO <sub>2</sub> -WACF-750	531.0	13.09	532.3	66.75	533.6	20.16
Mn–N/TiO <sub>2</sub> -WACF-850	531.1	14.54	532.0	64.44	533.5	21.02





**Figure 6** UV-Vis diffuse reflectance spectra (a–e) and band gap energy (f) of Mn-N/TiO<sub>2</sub>-WACF prepared at different temperatures.

insufficient at the lower calcination temperature. Mn-N/TiO<sub>2</sub>-WACF-650 samples have a complete anatase structure with high photocatalytic activity and show

the strongest absorption. The absorption decreases, however, when a calcination temperature of 750 °C is used. This trend is consistent with a reduction in Mn

and N content with a calcination temperature of 750 °C that is observed in the XPS analysis. This result suggests that the influence of Mn, N co-doping on rutile TiO<sub>2</sub> is weaker than that on anatase, which may be due to the superior symmetry of the rutile grain in comparison with anatase. Mn and N do not easily enter rutile TiO<sub>2</sub> because of its stable lattice structure. The band gap energy ( $E_g$ ) of the samples is estimated from the UV absorption spectra. As shown in Fig. 6f, the value of  $E_g$  is obtained using the following formula:

$$E_g = 1240/\lambda_g \quad (4)$$

where  $\lambda_g$  is the wavelength (nm) of the excitation light.

The onset absorption wavelength and corresponding band gap energies of all the samples, as obtained from the UV–Vis spectra, are summarized in Table 5. Mn and N-doping reduces the band gap energy for all doped samples in comparison with pure anatase TiO<sub>2</sub> (band gap width of 3.2 eV). The greatest decrease is seen when the sample is calcined at 650 °C, because the samples of Mn–N/TiO<sub>2</sub>-WACF-650 exhibit a crystal phase transformation from anatase to rutile. This is ascribed to co-dopants Mn and N do not easily enter the stable lattice structure of the rutile phase, the band gap energy increases. The absorption edge of the samples redshifts toward the visible light region (395–416 nm), suggesting that doped Mn and N significantly extend the absorption range of TiO<sub>2</sub> to the visible light region.

### PL analysis

PL spectroscopy is used to study the recombination of the generated photoinduced electron–hole pairs and the charge trapping efficiencies of the prepared semiconductor samples. As shown in Fig. 7, the spectra of all the samples are similar and do not exhibit new peaks when doped with Mn and N. This indicates that the doped Mn and N have been transformed completely via calcination. The most

intense PL emission peak is recorded at 410 nm, and correlates to the band–band PL phenomenon [33]. Furthermore, the intensity of the peaks in the samples decreases in the order Mn–N/TiO<sub>2</sub>-WACF-750 < Mn–N/TiO<sub>2</sub>-WACF-650 < Mn–N/TiO<sub>2</sub>-WACF-550 < Mn–N/TiO<sub>2</sub>-WACF-850 < Mn–N/TiO<sub>2</sub>-WACF-450, which can be attributed to the movement of photoexcited electrons from the THS conduction band to the metal centers, thereby inhibiting the recombination of electron–hole pairs and allowing an increase in photocatalytic activity [34–36].

### Effects of preparation conditions on the degradation rate of MB

The photocatalytic activity is evaluated by studying the degradation of a dye, namely, MB, under visible light irradiation, and the results are shown in Fig. 8. As the irradiation time increases, the degradation of all the samples increases gradually. Figure 8 reveals that 99% of MB is decolorized in the presence of Mn–N/TiO<sub>2</sub>-WACF-550 over 120 min. However, only 34, 24 and 49% of MB is removed after 240 min by samples calcined at 450, 750 and 850 °C, respectively. In the presence of Mn–N/TiO<sub>2</sub>-WACF-650, the MB is

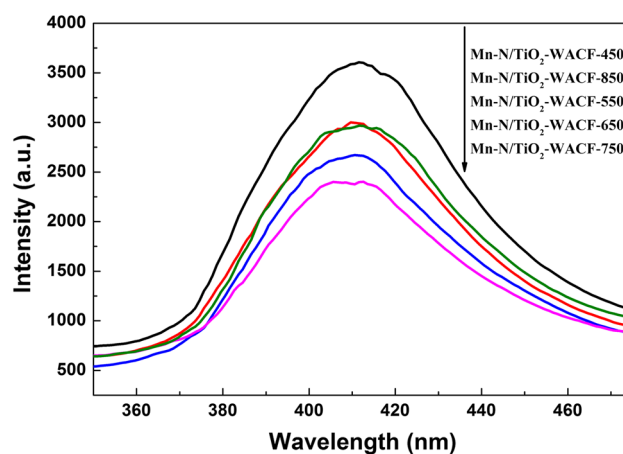


**Figure 7** PL spectra of Mn–N/TiO<sub>2</sub>-WACF prepared at different temperatures.

**Table 5** Summary of onset absorption wavelengths and band gap energies of Mn–N/TiO<sub>2</sub>-WACF

Samples	Mn–N/TiO <sub>2</sub> -WACF-450	Mn–N/TiO <sub>2</sub> -WACF-550	Mn–N/TiO <sub>2</sub> -WACF-650	Mn–N/TiO <sub>2</sub> -WACF-750	Mn–N/TiO <sub>2</sub> -WACF-850
Onset absorption wavelength, $\lambda_g$ (nm)	406	415	416	407	395
Band gap energy (eV)	3.05	2.99	2.98	3.05	3.14

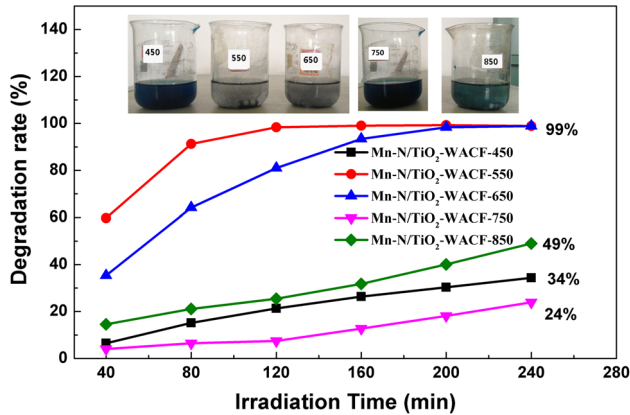


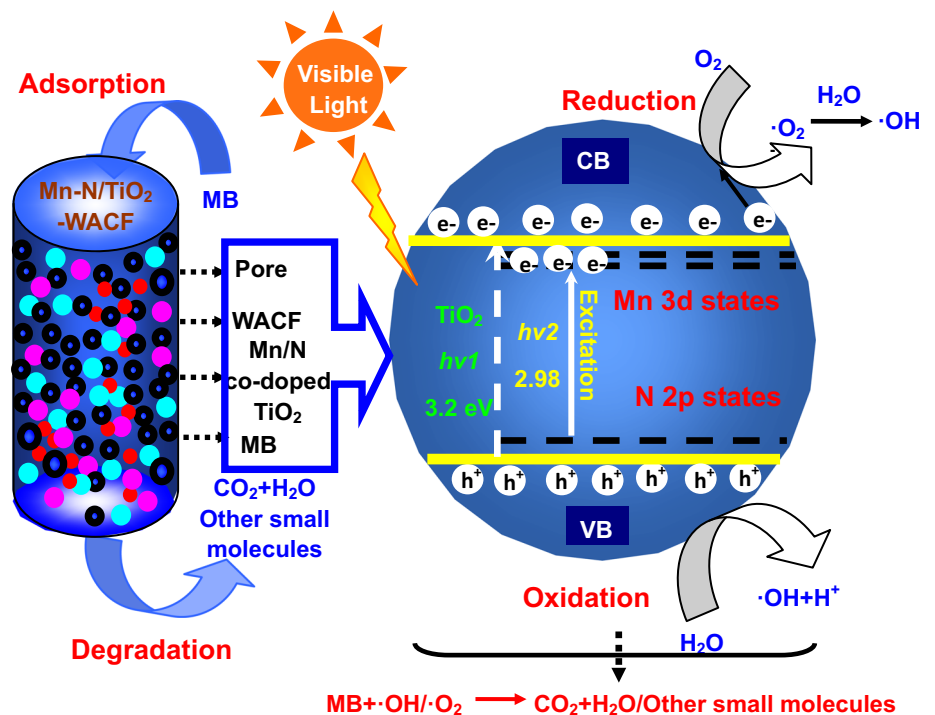
**Figure 8** Effect of irradiation time on the degradation rate of MB of Mn-N/TiO<sub>2</sub>-WACF.

also almost completely degraded over 200 min. Mn-N/TiO<sub>2</sub>-WACF-550 shows the best photocatalytic properties. Notably, when the calcination temperature is too high or too low, the efficiency of the photocatalyst decreases. This is mainly because at low calcination temperature, the growth of TiO<sub>2</sub> particles is insufficient, and the loading rate is not favorable for photocatalysis. The low photocatalytic activity of Mn-N/TiO<sub>2</sub>-WACF-450 can also be attributed to the high rate electron-hole pair recombination, which is supported by the PL analysis.

Meanwhile, when the calcination temperature is too high, the structure of the TiO<sub>2</sub> phase is unstable, and easily transforms from anatase to rutile. As a result, it is not suitable for the photocatalytic reaction. The degradation rate of MB for Mn-N/TiO<sub>2</sub>-WACF-850 is higher than that of Mn-N/TiO<sub>2</sub>-WACF-750, which may be a result of increased pore formation in WACF at increased calcination temperature, which offsets the negative photocatalytic effects from TiO<sub>2</sub> degradation at high temperature.

The catalytic mechanism under visible light irradiation is shown in Fig. 9. When the TiO<sub>2</sub> absorption energy is greater than  $E_g$  under irradiation with visible light, photogenerated electrons ( $e^-$ ) in the valence band (VB) of TiO<sub>2</sub> transfer to the conduction band (CB); meanwhile, holes ( $h^+$ ) are created in the VB. The doped Mn and N can not only reduce the band gap energy, but can also decrease the recombination rate of photogenerated electrons and photogenerated holes, increasing the photocatalytic activity of Mn-N/TiO<sub>2</sub>-WACF. Because the electrons are strong reducing agents and the holes are strong oxidizers, a series of reactions can occur with O<sub>2</sub> and H<sub>2</sub>O (Fig. 9). Finally, organic contaminants are oxidized and decomposed into CO<sub>2</sub>, H<sub>2</sub>O or other small molecules.

**Figure 9** Photocatalytic principle of Mn-N/TiO<sub>2</sub>-WACF under visible light irradiation.



## Conclusions

In this study, Mn–N/TiO<sub>2</sub>-WACF was successfully synthesized by a sol–gel and impregnation method. A supported photocatalyst with relatively small nanoparticles (23–33 nm) of TiO<sub>2</sub> was obtained with an anatase crystal phase (except for Mn–N/TiO<sub>2</sub>-WACF-850). Doped Mn and N significantly inhibited the transformation of TiO<sub>2</sub> from the anatase crystal phase to the rutile phase. Carbon was the most abundant element, and new N–Ti–N bonds were observed due to the substitution of oxygen atoms in the N-doped TiO<sub>2</sub> lattice. The UV–Vis spectra exhibited enhanced absorption in the visible light region. Compared to pure anatase TiO<sub>2</sub>, Mn/N co-doped TiO<sub>2</sub> showed a clearly reduced band gap energy. The carrier recombination rate was lowest for Mn–N/TiO<sub>2</sub>-WACF-750, as evidenced by the PL spectra, resulting in an increase in the photocatalytic activity for this sample. The choice of calcination temperature had a strong effect on the photocatalytic activity of the resultant Mn–N/TiO<sub>2</sub>-WACF. At a calcination temperature of 550 °C and an irradiation time of 120 min, the doped material demonstrated superior photocatalytic activity for the degradation of MB (99%). Hence, the present work provides insights into the design and fabrication of new low cost, high efficiency, robust photocatalytic materials for solving the wastewater from the printing and dye.

## Acknowledgements

The research was financially supported by National Natural Science Foundation of PR China (No. 31270607); Tianjin City Education Commission Research Fund Planning Project (Natural Science) (No. 2017KJ032); and Opening Project Fund of Key Laboratory of Rubber Biology and Genetic Resource Utilization, Ministry of Agriculture/State Key Laboratory Breeding Base of Cultivation & Physiology for Tropical Crops/Danzhou Investigation & Experiment Station of Tropical Crops, Ministry of Agriculture (RRI-KLOF201801).

## Compliance with ethical standards

**Conflict of interest** The authors declare that there is no conflict of interests regarding the publication of this article.

## References

- [1] Divya N, Bansal A, Jana AK (2013) Nano-photocatalysts in the treatment of colored wastewater. *Mater Sci Forum* 734:349
- [2] Reddy PAK, Reddy PVL, Kim KH, Kumar MK, Manvitha C (2017) Novel approach for the synthesis of nitrogen-doped titania with variable phase composition and enhanced production of hydrogen under solar irradiation. *J Ind Eng Chem* 53:253–260
- [3] Sreethawong T, Junbua C, Chavadeja S (2009) Photocatalytic H<sub>2</sub> production from water splitting under visible light irradiation using Eosin Y-sensitized mesoporous-assembled Pt/TiO<sub>2</sub> nanocrystal photocatalyst. *J Power Sources* 190:513–524
- [4] Qi XH, Zhuang YY, Yuan YC, Gu WX (2001) Decomposition of aniline in supercritical water. *J Hazard Mater* 90:51–62
- [5] Touati A, Hammedi T, Najjar W, Sayadi S, Ksibi Z (2016) Photocatalytic degradation of textile wastewater in presence of hydrogen peroxide: effect of cerium doping titania. *J Ind Eng Chem* 35:36–44
- [6] Liu XY, Ma XJ, Zhu LZ, Li DN (2015) Photocatalysis, microstructure, and surface characterization of TiO<sub>2</sub>-loaded wooden-activated carbon fibers. *Polym Compos* 36:62–68
- [7] Li SG, Guo YW, Zhang L, Wang J, Li Y (2014) Visible-light photocatalytic activity of Pt supported TiO<sub>2</sub> combined with up-conversion luminescence agent (Er<sup>3+</sup>:Y<sub>3</sub>Al<sub>5</sub>O<sub>12</sub>) for hydrogen production from aqueous methanol solution. *J Power Sources* 252:21–27
- [8] Zhou J, Zhu BB, Wang L (2017) Enhanced photocatalytic activity of Fe-doped TiO<sub>2</sub> coated on N-doped activated carbon composites for photocatalytic degradation of dyeing wastewater. In: International conference on materials science
- [9] Yang HM, Park SJ (2017) A study on photocatalytic behaviors of activated carbon fibers impregnated with n-doped titania. *J Nanosci Nanotechnol* 17:7593–7597
- [10] Pham TD, Lee BK (2017) Novel capture and photocatalytic conversion of CO<sub>2</sub> into solar fuels by metals co-doped TiO<sub>2</sub> deposited on PU under visible light. *Appl Catal A* 529:40–48
- [11] Wang C, Hu Q, Huang J, Wu L, Deng Z, Liu Z, Liu Y, Cao Y (2013) Efficient hydrogen production by photocatalytic water splitting using N-doped TiO<sub>2</sub> film. *Appl Surf Sci* 283:188–192
- [12] Appavu B, Kannan K, Thiripuranthagan S (2016) Enhanced visible light photocatalytic activities of template free mesoporous nitrogen doped reduced graphene oxide/titania composite catalysts. *J Ind Eng Chem* 36:184–193
- [13] Tang J, Wang J, Shrestha LK, Hossain MSA, Allothman ZA (2017) Activated porous carbon spheres with customized

- mesopores through assembly of diblock copolymers for electrochemical capacitor. *ACS Appl Mater Interface* 9:18986–18993
- [14] Huang YX, Peng LL, Liu Y, Zhao G, Chen JY (2016) Biobased nano porous active carbon fibers for high-performance supercapacitors. *ACS Appl Mater Interface* 8:15205–15215
- [15] Huang YX, Liu Y, Zhao GJ, Chen JY (2017) Sustainable activated carbon fiber from sawdust by reactivation for high-performance supercapacitors. *J Mater Sci* 52:478–488. <https://doi.org/10.1007/s10853-016-0347-0>
- [16] Yu XY, Wang SH, Zhang J (2017) Preparation of high adsorption performance activated carbon by pyrolysis of waste polyester fabric. *J Mater Sci* 53:1–9. <https://doi.org/10.1007/s10853-017-1928-2>
- [17] Li DN, Ma XJ (2014) Preparation and photocatalytic property of nano-TiO<sub>2</sub> loaded activated carbon fibers from liquefied wood. *Wood Res Slovak* 59:77–84
- [18] Yang JB, Mi HW, Luo S, Li YL, Zhang PX, Sun LN, Ren XZ (2017) Atomic layer deposition of TiO<sub>2</sub> on nitrogen-doped carbon nanofibers supported Ru nanoparticles for flexible LiO<sub>2</sub> battery: a combined DFT and experimental study. *J Power Sources* 368:88–96
- [19] Hu ZH, Xu T, Fang BW (2017) Photocatalytic degradation of vehicle exhaust using Fe-doped TiO<sub>2</sub> loaded on activated carbon. *Appl Surf Sci* 420:34–42
- [20] Chen J, Qin YF, Chen ZH, Yang Z, Yang WB, Wang YP (2016) Gas circulating fluidized beds photocatalytic regeneration of I-TiO<sub>2</sub> modified activated carbons saturated with toluene. *Chem Eng J* 293:281–290
- [21] Ma XJ, Zhou WR, Chen Y (2017) Structure and photocatalytic properties of Mn-doped TiO<sub>2</sub> loaded on wood-based activated carbon fiber composites. *Materials* 10:631
- [22] Li DN, Ma XJ, Liu XY, Yu LL (2013) Preparation and characterization of nano-TiO<sub>2</sub> loaded bamboo-based activated carbon fibers by H<sub>2</sub>O activation. *BioResources* 9:602–612
- [23] Ma XJ, Zhao GJ (2011) Variations in the microstructure of carbon fibers prepared from liquefied wood during carbonization. *J Appl Polym Sci* 121:3525–3530
- [24] Li DN, Ma XJ (2013) Preparation and characterization of activated carbon fibers from liquefied wood. *Cellulose* 20:1649–1656
- [25] Ma XJ, Zhang F, Wei LQ (2015) Effect of wood charcoal contents on the adsorption property, structure, and morphology of mesoporous activated carbon fibers derived from wood liquefaction process. *J Mater Sci* 50:1908–1914. <https://doi.org/10.1007/s10853-014-8754-6>
- [26] Hanaor DAH, Sorrell CC (2011) Review of the anatase to rutile phase transformation. *J Mater Sci* 46:855. <https://doi.org/10.1007/s10853-010-5113-0>
- [27] Gu Y, Huang J (2013) Precise size control over ultrafine rutile titania nanocrystallites in hierarchical nanotubular silica/titania hybrids with efficient photocatalytic activity. *Chemistry* 19:10971–10981
- [28] Bourgeois S, Seigneur PL, Perdereau M (1995) Study by XPS of ultra-thin nickel deposits on TiO<sub>2</sub> (100) supports with different stoichiometries. *Surf Sci* 328:105–110
- [29] Wahid M, Parte G, Phase D, Ogale S (2015) Yogurt: a novel precursor for heavily nitrogen doped supercapacitor carbon. *J Mater Chem A* 3:1208–1215
- [30] Chiang YC, Chen YJ, Wu CY (2017) Effect of relative humidity on adsorption breakthrough of CO<sub>2</sub> on activated carbon fibers. *Materials* 10:1296
- [31] Yang S, Lin Y, Song X, Zhang P, Gao L (2015) Covalently coupled ultrafine H-TiO<sub>2</sub> nanocrystals/nitrogen-doped graphene hybrid materials for high-performance supercapacitor. *ACS Appl Mater Interfaces* 7:17884–17892
- [32] Li Y, Wang Z, Lv XJ (2014) N-doped TiO<sub>2</sub> nanotubes/N-doped graphene nanosheets composites as high performance anode materials in lithium-ion battery. *J Mater Chem A* 2:15473–15749
- [33] Huang W, Tang X, Wang Y, Kolytyn Y, Gedanken A (2000) Selective synthesis of anatase and rutile via ultrasound irradiation. *Chem Commun* 15:1415–1416
- [34] Yu J, Ma T, Liu S (2011) Enhanced photocatalytic activity of mesoporous TiO<sub>2</sub> aggregates by embedding carbon nanotubes as electron-transfer channel. *Phys Chem Chem Phys* 13:3491–3501
- [35] Choi S, Kim S, Lim S, Park H (2010) Photocatalytic comparison of TiO<sub>2</sub> nanoparticles and electrospun TiO<sub>2</sub> nanofibers: effect of mesoporosity and interparticle charge transfer. *J Phys Chem C* 114:16475–16480
- [36] Seadira TWP, Sadanandam G, Ntho T, Masuku CM, Scurrill MS (2018) Preparation and characterization of metals supported on nanostructured TiO<sub>2</sub> hollow spheres for production of hydrogen via photocatalytic reforming of glycerol. *App Catal B Environ* 222:133–145